



Reducing the excess energy offset in organic/inorganic hybrid solar cells: Toward faster electron transfer



Qinghua Li^{a,*}, Xiao Jin^a, Xuwei Yang^a, Changyong Chen^a, Zihan Chen^a, Yuancheng Qin^a, Tai-huei Wei^b, Weifu Sun^{c,*}

^a Key Laboratory of Jiangxi Province for Persistent Pollutants Control and Resources Recycle, Nanchang Hangkong University, Nanchang 330063, PR China

^b Department of Physics, National Chung-Cheng University, Chia-Yi 621, Taiwan, ROC

^c School of Materials Science and Engineering, The University of New South Wales, Sydney, NSW 2052, Australia

ARTICLE INFO

Article history:

Received 6 May 2014

Received in revised form 9 July 2014

Accepted 13 July 2014

Available online 22 July 2014

Keywords:

Silver doping

Energy level control

Organic/inorganic hybrid solar cells

Photoexcited electron transfer

ABSTRACT

The photoexcited electron transfer rate represents one of the most important properties required for photovoltaic devices. However, the fabrication of solar cells with a faster electron transfer remains a technological challenge. Regulating the energy level alignment of acceptor-donor system by the incorporation of foreign ions is one of the most promising strategies to achieve this aim. Herein we demonstrate that the incorporation of silver ions into TiO₂ nanocrystals results in a remarkable reduction of energy offset between the conduction band edge of acceptor and the lowest unoccupied molecular orbital of donor. In particular, the electron transfer life time was shortened from 30.2 to 18.3 ps, i.e., almost 40% faster than pure TiO₂ acceptor, thus leading to a notable enhancement of power conversion efficiency by almost 38% in organic/inorganic hybrid solar cells. The reduction of the 'excess' energy offset accelerates the electron transfer, which is expected to have an important role in applications of solar energy conversion and photon detectors.

© 2014 Elsevier B.V. All rights reserved.

1. Introduction

Organic/inorganic hybrid solar cells (HSCs) are one of the promising candidates to provide clean energy owing to their low cost, simple architecture and flexible solar modules [1]. These HSCs are capable of exploiting the unique advantageous properties of both types of materials such as low-temperature solution-processing of organic semiconductors and high electron mobility of inorganic semiconductors [2]. As one of the newly emerging hotspots, HSCs based on the well-known conducting polymer poly(3-hexylthiophene) (P3HT) have attracted much attention [1,3–7] thus far. Despite recent advances, the fabrication of low-cost and high power conversion efficiency (PCE) HSCs remains a technological challenge. Over the past five years, most of the P3HT-based organic/inorganic HSCs have demonstrated a PCE ranging from 1% to 3%, depending on the type of the inorganic nanocrystals, their morphologies, shapes, and others [3,8–10]. Many attempts have been made to enhance the performances of HSCs by controlling the size, shape and morphologies of the semiconductors, utilizing low

band gap organic materials, or introducing buffer layers [11–14], etc. Among them, one facile and efficient approach is to introduce foreign metal ions (such as Ag, Ni, Mo, Cr, Co, etc.) into inorganic semiconductors [15–20]. Ag-doped titanium dioxide (TiO₂), being considered as a promising photocatalytic material [21–23], has drawn considerable attention in solar cells [24–26]. On one hand, Ag–TiO₂ nanocomposites have exhibited intriguing properties thus far, including the increased scattering, the enhanced solar light harvest by broadening the photo response of TiO₂ from the ultra-violet (UV) to visible light, the improved anatase crystallinity and the boosted conductivity of the TiO₂ electrodes and also the inhibited recombination of the photoexcited carriers, etc. These merits of Ag–TiO₂ nanocomposites have been widely documented in literatures [24,26–28]. On the other hand, the silver ion does not damp out the plasmon mode as strongly as other metals because its d–s band gap falls within the ultraviolet visible (UV–vis) region [29]. Therefore, Ag-decorated TiO₂ photocatalyst holds great promise in the applications of solar energy.

Although Ag-doped TiO₂ nanocrystals have exhibited excellent characteristics, nonetheless the origin of the intrinsic driving force behind the excellent performances remains unknown. What is more, the inefficient charge separation and the strong geminate recombination [30] within the bulk heterojunction (BHJ) remain

* Corresponding author. Tel.: +86 791 83953468; fax: +86 791 83953468.

E-mail addresses: qhli@hqu.edu.cn (Q. Li), weifu.sun518@gmail.com (W. Sun).

the bottlenecks for the ultimate device performance [9]. These open questions and existing problems motivate us to promote the dissociation of photogenerated electron–hole pairs and to accelerate the charge transport rate. Because the charge transfer rate of photoexcited electron/hole at the interface of BHJ during the charge photogeneration is one of the key factors influencing the device performance [31]. Herein, an effective strategy to overcome these obstacles is to incorporate the silver ions into the inorganic semiconductors. However, the crucial role of energy level regulation induced by Ag-modified TiO_2 and the complicate photoexcited electron transport dynamics at the interface of donor and acceptor have not yet been clarified. Therefore, silver-doped TiO_2 nanocrystals were first synthesized using the hydrothermal method in this work and then employed to control the energy level of acceptor. Finally, the effects of Ag doping on the energy level regulation, photoexcited charge carrier transfer and the photovoltaic device performances were examined by cyclic voltammetry (CV), steady-state photoluminescence (PL) and transient PL spectroscopies, etc.

2. Experimental

2.1. Materials

All analytical purity chemical reagents including tetrabutyl titanate, silver nitrate (AgNO_3), polyethylene glycol (PEG, molecular weight of 20,000), acetonitrile, nitric acid, acetic acid, P25 (Degussa), isopropanol, tetrabutyl-ammonium hexafluorophosphate (TBAPF_6), OP emulsifying agent (Triton X-100), methylbenzene, conjugated polymer P3HT and poly(3,4-ethylenedioxythiophene)-polystyrene sulfonic acid (PEDOT:PSS) were purchased from Sigma–Aldrich Ltd., Hongkong, China except where otherwise indicated. Fluorine-doped tin oxide glass (FTO, $8 \Omega \text{ cm}^{-2}$) was purchased from Hartford Glass Co., USA.

2.2. Synthesis of Ag-doped TiO_2 colloid

The Ag-doped TiO_2 colloid was prepared by a minor modification of the hydrothermal method [32,33]. Tetrabutyl titanate (10 mL) was added to distilled water (100 mL) under stirring, followed by a white precipitate immediately. Then, 5 mL of 1 M AgNO_3 water solution was added into the tetrabutyl titanate solution. After that, the precipitate was filtered, washed with distilled water, and then transferred to a mixed solution (150 mL) containing nitric acid (1 mL) and acetic acid (10 mL) at 80°C . Under vigorous stirring, a light blue Ag-doped TiO_2 precursor was formed, followed by an ultrasonic stirring for 30 min. Finally, the mixture was hydrothermally treated in an autoclave at 200°C for 24 h to form a colloid of Ag-doped TiO_2 . Subsequently, the P25 (0.075 g) and OP emulsifying agent (1 mL) were dispersed into the colloid by ultrasonically vibrating for 90 min and hydrothermally treating at 200°C for 12 h to form a white colloid. At last, the resultant slurry was concentrated to 1/5 of its original volume by a thermal evaporation, and PEG-20000 (0.5 g) and a few drops of the Triton X-100 emulsification reagent were added, finally an even and stable Ag-doped TiO_2 colloid was produced.

2.3. Fabrication of HSC

A layer of Ag-doped TiO_2 acceptor film with a thickness of 200 nm was prepared by coating the Ag-doped TiO_2 colloid on FTO glass using spin-coating technique, followed by sintering in air at 450°C for 30 min. Then the acceptor film was soaked in a 0.15 M P3HT methylbenzene solution for 12 h to uptake P3HT for the fabrication of BHJ. Next, the PEDOT:PSS layer was spin-coated onto the

BHJ. Finally, Pt electrode was deposited on the top of the PEDOT:PSS layer by thermal evaporation under vacuum.

2.4. Characterizations

The morphology of acceptor layers were characterized by using a field emission scanning electron microscope (FE-SEM, Hitachi S4800, Japan). The cross-section samples for SEM characterization were prepared by breaking a HSC anode in half. Elemental analysis was conducted using Genesis energy dispersive spectrum (EDS) software. The CV and electrochemical impedance spectroscopy (EIS) results were obtained using a BAS 100B instrument (BASi Inc., USA) at room temperature and at a scan rate of 50 mV s^{-1} with 0.1 M TBAPF_6 in acetonitrile as the supporting electrolyte, a platinumized platinum (1.0 cm^2) as the counter electrodes, and Ag/Ag^+ electrode as the reference electrode. The crystalline structures of the samples were characterized by X-ray diffraction (XRD) patterns on a X-ray diffractometer (MiniFlex II, Rigaku Ltd., Japan) using $\text{Cu K}\alpha$ radiation ($\lambda = 0.154 \text{ nm}$) at 50 kV and 250 mA at room temperature. X-ray photoelectron spectrum (XPS) measurements were performed using an Al $\text{K}\alpha$ X-ray source on a multifunctional imaging electron spectrometer (Thermo ESCALAB 250XI, USA). The residual concentration of silver ions was monitored by inductively coupled plasma atomic emission spectroscopy (ICP-AES, Leeman Co., USA, PROFILE SPEC). The PL spectrum was measured by using a spectrophotometer (FLS920, Edinburgh, UK), in which a xenon lamp and a photomultiplier tube (R955, Hamamatsu, Japan) were used as excitation source and fluorescence detector, respectively. The photocurrent–voltage (J – V) curves of the assembled HSCs were recorded on an Electrochemical Workstation (Xe Lamp Oriel Sol3A™ Class AAA Solar Simulators 94023A, USA) under irradiation of a simulated solar light from a 100 W xenon arc lamp in ambient atmosphere, which was calibrated using a Newport-certified single crystal silicon solar cell.

Charge Photogeneration Dynamics: Transient PL measurements were carried out on a spectrometer (250IS/SM, Bruker Optics, Germany) with intensified charge coupled device detector (IStar740, Andor, UK). The samples were excited by 120 fs laser pulses at 400 nm with a repetition rate of 10 Hz. The time resolution of this experiment was determined to be $\sim 60 \text{ ps}$. Transient absorption spectrum (TAS) measurements of the BHJs were performed by the mode-locked Ti:sapphire laser (Mira 900, Coherent Inc., USA) in combination with a regenerative amplifier (Legend-F, Coherent Inc., USA). The ultrafast light source with a temporal resolution of $\sim 120 \text{ fs}$ was generated by a mode-locked titanium-sapphire laser operating at 800 nm. Each data was obtained by averaging 100 individual measurements to improve the signal-to-noise ratio (SNR), and the typical detection sensitivity of the difference absorption (ΔOD) was better than 10^{-4} .

3. Results and discussion

3.1. Characterizations of acceptors

The XRD patterns of Ag-doped TiO_2 and bare TiO_2 nanocrystals calcined at 450°C are shown in Fig. 1A. Both of the samples exhibit the identical diffraction peaks at 25.48° , 37.75° and 48.01° , corresponding to the distance spacings of 3.51, 2.37 and 1.89 \AA , respectively, which can be indexed as the anatase phase of TiO_2 (JCD 01-084-1286). In addition, a typical but weak peak at 27.443° was also observed for both of the samples, implying the presence of the rutile phase (JCD 00-001-1292) with the corresponding d -space of $d = 3.25 \text{ \AA}$. In short summary, it was revealed from the XRD patterns that the prepared nanocrystals are predominantly anatase phase TiO_2 with only a small amount of rutile phase TiO_2 .

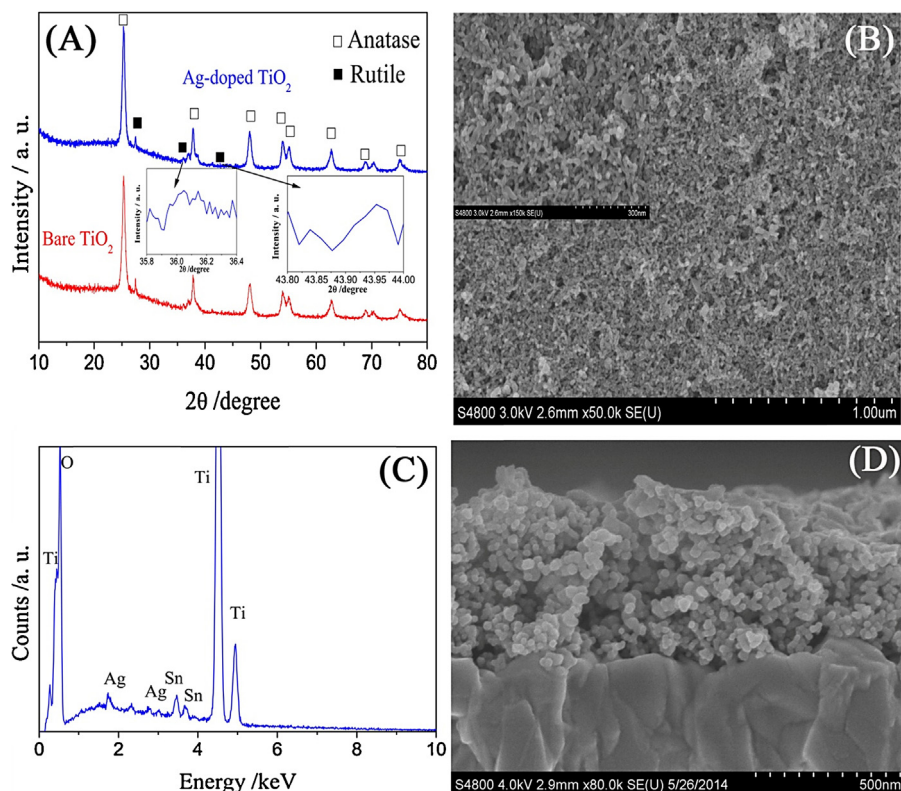


Fig. 1. (A) XRD patterns of bare TiO₂ and Ag-doped TiO₂ and the insets highlight the peaks at 36.1° and 41.9°; (B) SEM image of Ag-doped TiO₂ nanoparticles coated on FTO glass and the inset shows the products at high magnification; (C) EDS analysis of Ag-doped TiO₂ electrode; (D) Cross-sectional SEM image of Ag-doped TiO₂ film.

According to the standard cards of anatase and rutile phases of TiO₂, it is found that the most typical characteristics peaks of rutile that are not overlapped with those of anatase are 27.4°, 36.1° and 43.9°. But as observed from the XRD pattern, the only obviously appreciable peak that can be assigned to rutile phase TiO₂ was at around 27.44°; besides, the other two peaks at 36.1° and 43.9° have been highlighted in the insets of Fig. 1A. However, in order to have a relatively accurate quantitative estimation of contents of rutile phase TiO₂, thus according to the integral area under the peaks at 27.43°, 36.1° and 43.9° relative to the total area, the content of rutile phase TiO₂ is estimated to be about 1.21% and the contents of anatase phase TiO₂ is about 98.79%. Note that a small amount of the rutile phase is prone to lead to a higher PCE thanks to the enhancement of light harvesting stemming from the superior light-scattering characteristics [24,26,34,35]. It is also worth mentioning that during the hydrothermal preparation of Ag-doped TiO₂, since Ag ions were completely dissolved and mixed together with TiO₂, followed by thoroughly washed by distilled water, some of the Ag species can be well dispersed or doped into the TiO₂ nanoparticles. However, the Ag species can be hardly observed from the XRD pattern at this stage, being subject to the rather small amount of an initial loading of Ag ions. As observed from Fig. 1B, the surface of the prepared Ag-doped TiO₂ acceptor layers clearly exhibits a porous structure, which favors the physical adsorption of P3HT molecules by trapping the solution in the microporomerics because of the intermolecular attractive forces [36–39]. Note that due to the rather small amount of an initial usage of Ag ions, the surface roughness can be assumed to be independent of Ag dopant. As the electron-extracting layer, the porous and loose nanostructure of Ag-doped TiO₂ film (particle size of ~20 nm in diameter as highlighted in the inset of Fig. 1B) will allow a large number of P3HT molecules to permeate into TiO₂ film and make for an intimate p–n contact as demonstrated in Fig. 1D, thus eventually benefiting solar light harvesting [40,41]. Besides,

the size of TiO₂ nanoparticles was also estimated using XRD data. According to the Debye–Scherrer equation $D = K\lambda / \beta \cos \theta$, where D is the average crystallite size, K is the shape factor, λ is the X-ray wavelength, β is the full-width of half-maximum of the peak and θ is the diffraction angle [42], the size of the TiO₂ nanoparticles calculated from XRD data is about 16.2 nm, which matches well with that (~20 nm) observed from the SEM image. To corroborate the doping of Ag species into TiO₂ nanoparticles, the EDS spectrum was measured and shown in Fig. 1C. It can be clearly observed that the elements Ag, O, Ti are present, revealing the successful incorporation of Ag ions into the TiO₂ nanoparticles.

However, the chemical state of the Ag species remains unknown, therefore XPS technique was employed to identify the chemical bonding state. Fig. 2A shows the full XPS spectra of the two samples, in which Ti, O, and C elements are clearly revealed, with sharp photoelectron peaks at the binding energies of 530 eV (O1s), 459 eV (Ti2p), and 285 eV (C1s). Besides, the Ag 3d peak (368 eV) is clearly revealed in XPS curve for Ag doped TiO₂ sample. In this work, although silver ion concentration is low, the signal from the Ag3d states is obvious, indicating that Ag species are largely dispersed onto the surfaces of anatase nanoparticles. The XPS spectrum confined to the Ag window (Fig. 2B) exhibits two peaks located at 373.7 and 367.7 eV for Ag-doped TiO₂, which can be mainly ascribed to the Ag 3d_{3/2} and 3d_{5/2} binding energies of Ag(I), respectively [43]. These results indicate that the Ag clusters predominantly exist in oxidized state. In contrast, no XPS peak of Ag 3d is observed in the bare TiO₂ as expected. Fig. 2C shows the small energy window with high resolution of the O1s band: both of the XPS spectra exhibit two peaks at 530.0 and 532.1 eV that are ascribed to Ti–O in TiO₂ bulk and the OH on the surface of TiO₂ [22]. It is worth mentioning that the samples were synthesized by hydrothermal treatment which may introduce hydroxyl on the surface; besides, one additional but weak peak at 529.4 eV is observed for Ag doped TiO₂, and this can

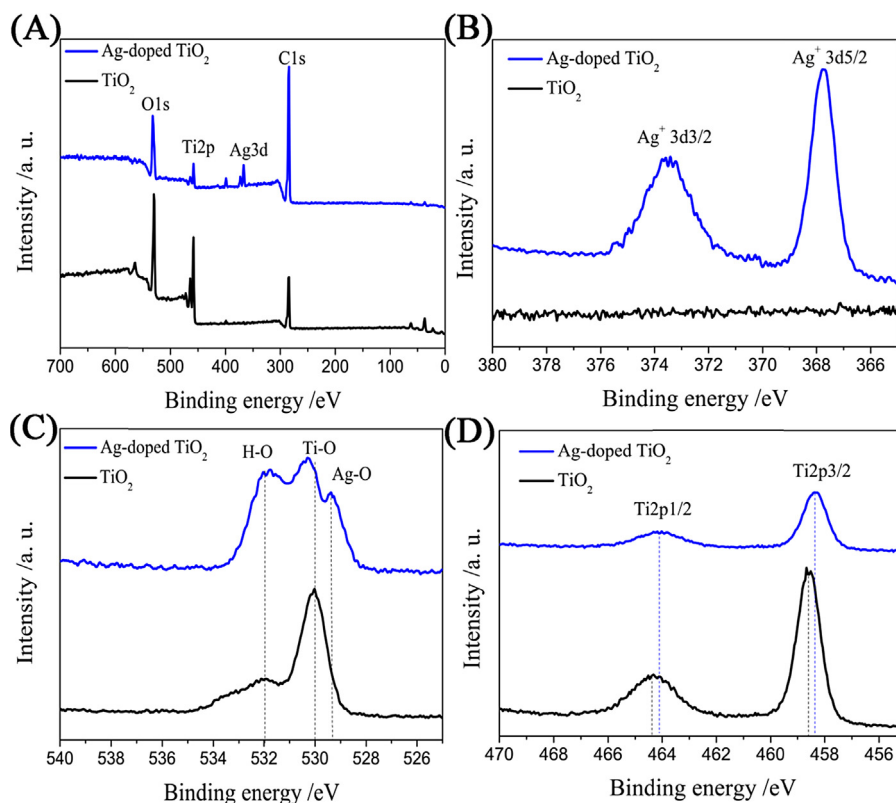


Fig. 2. The full XPS survey spectra (a); the Ag3d (b), O1s peaks (c) and Ti2p (d) peaks of Ag-doped TiO₂ and pure TiO₂.

be assigned to Ag–O binding energy, implying that the chemical state of Ag species should be in oxidized states Ag(I). In short summary, the Ag species should be predominantly oxidized species of Ag(I). This is consistent with the other hydrothermally prepared Ag-doped TiO₂ [23]. Furthermore, as shown in Fig. 2D, the Ti2p peaks of the bare TiO₂ locating at 458.6 and 464.4 eV can be assigned to the peaks of Ti2p_{3/2} and Ti2p_{1/2}, the 5.8 eV gap between the two states are attributed to the lattice of Ti in TiO₂ with 2p₃ binding energy of the Ti(IV) ion [44].

In order to figure out the final concentration of Ag ions in Ag-doped TiO₂, we tested transparent solution of the sample with Ag doping using ICP-AES. The AgNO₃ aqueous solution is used as standard liquid to determine the concentration of Ag ions in Ag-doped TiO₂. By linear fit of the ICP-AES peak intensity of standard liquid (Fig. 3A), the relationship between the peak intensity and the concentration is revealed in Fig. 3B. Then the residual concentration of silver ions prepared from the Ag-doped TiO₂ is derived to be 3.65 mg L^{−1}. Therefore, the final silver ion concentration in Ag–TiO₂ is about 0.23 wt%.

3.2. Photoexcited electron transfer in BHJs

To design the highly efficient HSCs, it is necessary to have a complete understanding of the underlying photophysical mechanism that governs their operation performance. In particular, the dynamics of photoexcited charge transfer at the interface of donor and acceptor call for in-depth probe. Therefore, time-integrated and time-resolved PL spectra were employed to investigate the photoexcited electron transfer [45]. Comparative studies on bare TiO₂/P3HT against Ag-doped TiO₂/P3HT BHJs enable the identification of the effect of Ag-doping on the electron transfer dynamics. Under the identical experimental conditions, the PL intensity is quenched more with Ag-doped TiO₂ than that with bare TiO₂ only (Fig. 4A). It is known that the PL spectrum of P3HT is sensitive to

the degree of the photoinduced electron transfer to the acceptor [46]: an efficient PL quenching is indicative of a high degree of the photoinduced electron transfer in Ag-doped TiO₂/P3HT BHJ. Since it is generally accepted that the PL lifetime allows one to estimate the photoinduced electron transfer rate within the BHJs [45–47]. In order to probe into the photoinduced electron transfer in BHJs, time-resolved single-photon counting PL experiments were performed to evaluate the lifetimes and then the PL decays for the three different films are shown in Fig. 4B. The films exhibit an instantaneous response near zero delay, which is well interpreted as auto correlation of laser pulse. The addition of either TiO₂ or Ag-doped TiO₂ results in a significant reduction of the PL lifetime, and obviously, the decays of the two blend films are much faster than that of neat P3HT film. The emissions for the two blend films were intensively quenched after approximately 300 ps, which can be attributed to the electron transfer from donor to acceptor. In contrast, for neat P3HT film, a single lifetime of 890 ps was obtained by exponentially fitting the transients. But for either TiO₂ or Ag-doped TiO₂ as an electron extraction layer, it can be clearly observed that the short-lived components dominate the transients: the relatively fast component (~70–80 ps) indicates that the PL spectrum of P3HT becomes overwhelmed by a fast electron transfer. Note that the obtained lifetimes in this work reasonably agree with the reported values [46,48–50]. However, because the time resolution of these measurements (~60 ps) is not high enough to resolve the fast electron transfer. Therefore, femtosecond transient absorption spectroscopy (TAS) with a temporal resolution of ~120 fs and a high SNR (10^{−4}) will be applied next to obtain the more detailed photoexcited electron transport dynamics.

Fig. 5 shows the TAS decays of BHJs based on pure TiO₂/P3HT and Ag-doped TiO₂/P3HT, respectively. For 400-nm (i.e., 3.1 eV) photoexcitation, the positive signals probed at 650 nm represent the photoinduced absorptions, which can be ascribed to the photoinduced excited-state absorption, i.e., the so-called state-filling effects

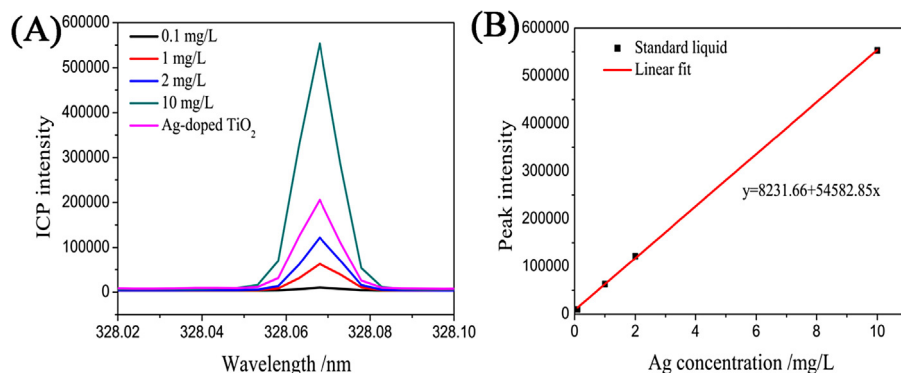


Fig. 3. (A) ICP spectrum of AgNO₃ aqueous solution (0.1, 1, 2 and 10 mg L⁻¹) and Ag-doped TiO₂ (0.4 g) dissolved in nitrohydrochloric acid (250 mL); (B) Linear fit of the ICP peak intensity of the standard AgNO₃ solution with Ag concentration.

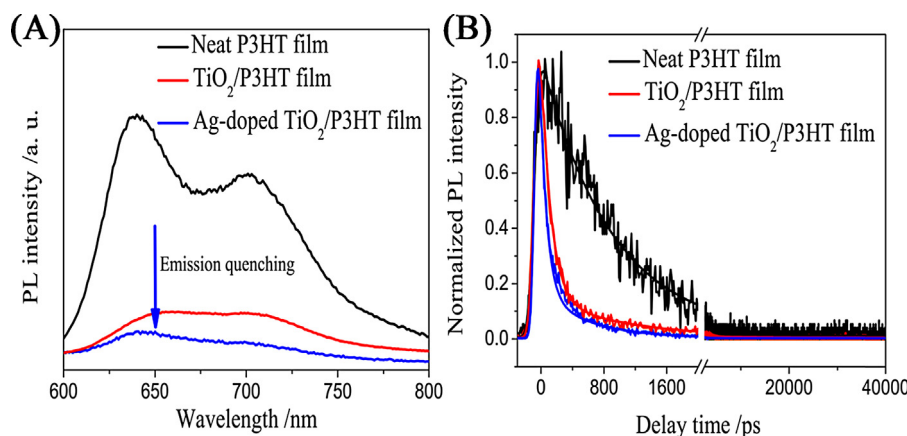


Fig. 4. Normalized femtosecond transient absorption decays of Ag-doped TiO₂/P3HT (open circle) and pure TiO₂/P3HT (solid square) BHJs, excited at 400 nm (17 μJ cm⁻²) and probed at 650 nm, respectively. Solid lines represent the fitting curves with exponential components.

[51–53]. Both of the curves in Fig. 5 exhibit four pathways of electron transports, including (i) an instantaneous response that is well interpreted by a scalar multiple of the laser pulse autocorrelation function, (ii) an ultrafast decay that represents the nonradiative decay of the hot electron in P3HT with a vibronic relaxation time of τ_{vib} (typically within 1 ps [31]), (iii) a fast transient that originates from the fast electron transfer at the interface of BHJs with a transfer time of τ_{fast} (on the order of ps [31]) and (iv) a long tail contributed by the geminate recombination [30] of the electron-hole pairs with a time constant τ_{re} (~ns [53,54]). The transient absorption data can be taken as a convolution of the background-free laser

pulse autocorrelation function $G(t)$ with the response function $\phi(t)$ [55,56]

$$S(\tau) = \int_{-\infty}^{+\infty} G(\tau - t)\phi(t) dt \quad (1)$$

where $\phi(t)$ is a linear superposition of electronic contributions. And $\phi(t)$ can be described with a superposition of the following contributions:

$$\phi(t) = \delta(t) + A \exp\left(-\frac{t}{\tau_{\text{vib}}}\right) + B \exp\left(-\frac{t}{\tau_{\text{fast}}}\right) + C \exp\left(-\frac{t}{\tau_{\text{re}}}\right) \quad (2)$$

where $\delta(t)$ is the purely electronic hyperpolarizability that responds instantaneously to the applied laser field. All the decays were well fitted using Eq. (2) and the fitted lifetime constants and amplitudes were summarized in Table 1. Strikingly, the fast electron transfer in Ag-doped TiO₂/P3HT (i.e., 18.3 ps) is much faster than pure TiO₂/P3HT (30.2 ps) BHJ. Moreover, the efficiency of the fast electron transfer can be estimated by the following relationship using the fitted amplitudes: $B/(A+B+C)$, i.e., 12.1% for TiO₂/P3HT and 14.9% for Ag-doped TiO₂/P3HT. Now one will wonder what is held responsible for the enhancement of the fast electron transfer. This may be closely related to the Ag dopant-induced energy level regulation of the acceptor TiO₂.

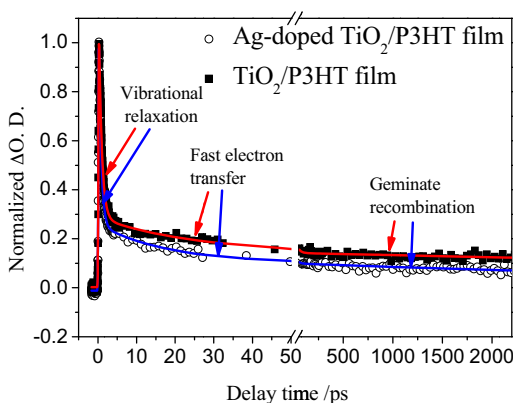


Fig. 5. Normalized femtosecond transient absorption decays of Ag-doped TiO₂/P3HT (open circle) and pure TiO₂/P3HT (solid square) BHJs, excited at 400 nm (17 μJ cm⁻²) and probed at 650 nm, respectively. Solid lines represent the fitting curves with exponential components.

3.3. Energy level formation in BHJs and device performances

The energy offset between the conduction band (CB) edge of acceptor (TiO₂) and the lowest occupied molecular orbital (LUMO)

Table 1

Lifetimes and the amplitudes fitted from TAS using the linear superposition of electronic contributions.

Lifetime (τ) (amplitude)	τ_{vib} (ps) (A)	τ_{fast} (ps) (B)	τ_{re} (ps) (C)
Ag-doped TiO ₂ /P3HT	0.60 ± 0.01 (0.93)	18.3 ± 1.2 (0.18)	7.3 ± 0.5 (0.10)
TiO ₂ /P3HT	0.74 ± 0.01 (0.95)	30.2 ± 1.0 (0.15)	14.0 ± 1.5 (0.14)

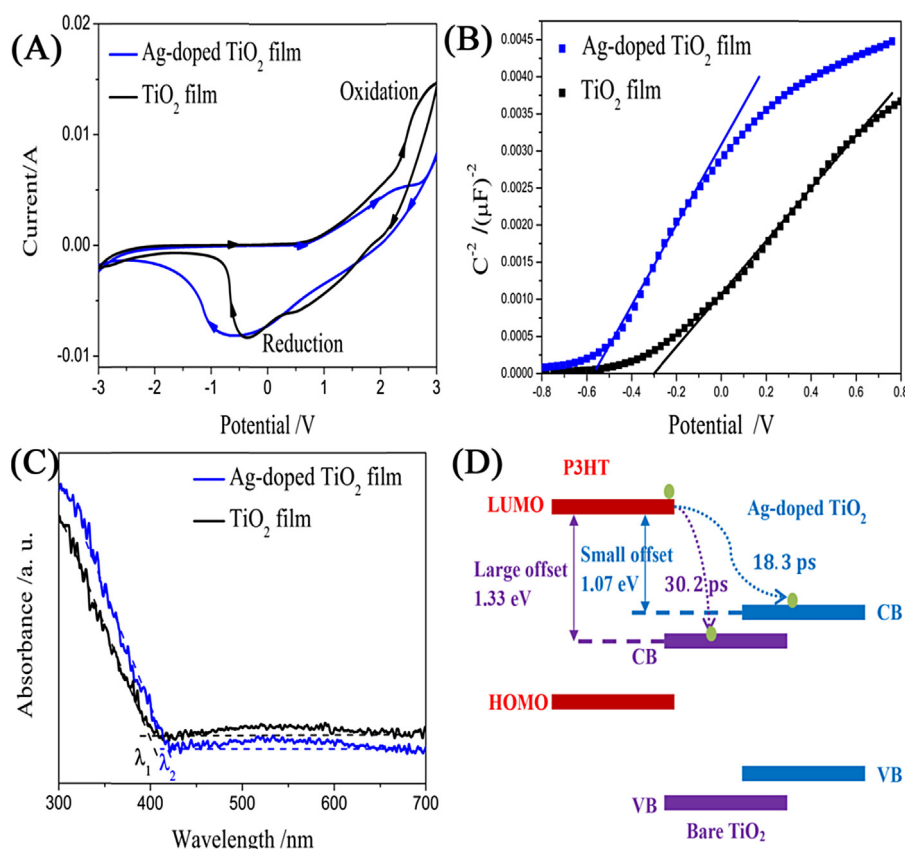


Fig. 6. (A) CV behaviors of bare TiO₂ and Ag-doped TiO₂ film in acetonitrile containing 0.1 M TBAPF₆ at a sweep rate of 50 mV s⁻¹; (B) Mott-Schottky plots of the different films. Mott-Schottky measurements were done at the frequency of 1 kHz in the aqueous solution of 0.05 M Na₂SO₄; (C) The UV-vis diffuse reflectance spectra of the three films; (D) The energy level diagram of the bulk heterojunctions with/without Ag doping.

of donor (P3HT), i.e., CB-LUMO offset, is ~ 1.33 eV, which enables to break the Coulomb attraction (typically 0.1–0.5 eV) [54] but not in an efficient way. Gong and his co-workers have demonstrated that an efficient charge transfer can be observed from BHJ even though the CB-LUMO energy offset is only 0.12 eV [57]. In a bid to reduce the CB-LUMO offset and minimize the energy loss in HSCs, our attention is paid to the tailoring of energy level of acceptor induced by Ag dopant. Therefore, the CV experiments were performed and the CV characteristics of the bare TiO₂ and Ag-doped TiO₂ films are shown in Fig. 6A. The energy levels of CB and valence band (VB) edges of acceptor can be calculated using the formula: CB (or VB) (eV) = $-4.8 - (E - E_{1/2})$ (eV), where E is a peak point of the redox potential [58], $E_{1/2}$ is the formal potential of F_c/F_c^+ system of 0.09 V ($E_{1/2} = 0.09$ V) against Ag/Ag⁺ system [59]. The positive and negative peaks at oxidation and reduction potentials correspond to the

VB and CB energy bands, respectively. The CB, VB and energy gap of both bare TiO₂ and Ag-doped TiO₂ nanocrystalline thin film electrodes are summarized in Table 2. The results show that the energy gap of acceptor is slightly affected only by Ag doping, whereas both the CB and VB energy levels of the acceptor have changed largely. In detail, the CB and VB energy levels have been elevated from -4.33 and -7.36 eV to -4.07 and -7.05 eV, respectively. After Ag doping, a notable reduction of the CB-LUMO offset is observed, i.e., from 1.33 to 1.07 eV in Fig. 6B. The reduction of excess CB-LUMO offset should be responsible for the shorter electron transfer lifetime at the interface of BHJ [57,60,61]. Therefore, the photoexcited electron transfer becomes more competitive than the geminate recombination [30]. Besides, Mott-Schottky plots along with UV-vis spectra were used to separately estimate the CB and VB energy levels of the different films. Mott-Schottky plots are

Table 2

Electrochemical parameters of the different films.

Films	E_{red}^a (V)/CB (eV)	E_{ox}^a (V)/VB (eV)	E_g^a (eV)	FB potential (V)/CB ^b (eV)	E_g^b (eV)	VB ^b (V)
TiO ₂	$-0.38/-4.33$	$2.65/-7.36$	3.03	$-0.30/-4.41$	3.04	-7.45
Ag-doped TiO ₂	$-0.64/-4.07$	$2.34/-7.05$	2.98	$-0.57/-4.14$	2.95	-7.09

^a Electrochemical parameters were obtained from CVs. The band gap E_g was calculated from the difference between VB and CB values.

^b The CB values were determined by Mott-Schottky plots and the band gap was estimated from the UV-vis spectrum, then the VB values were derived from CB and band gap values.

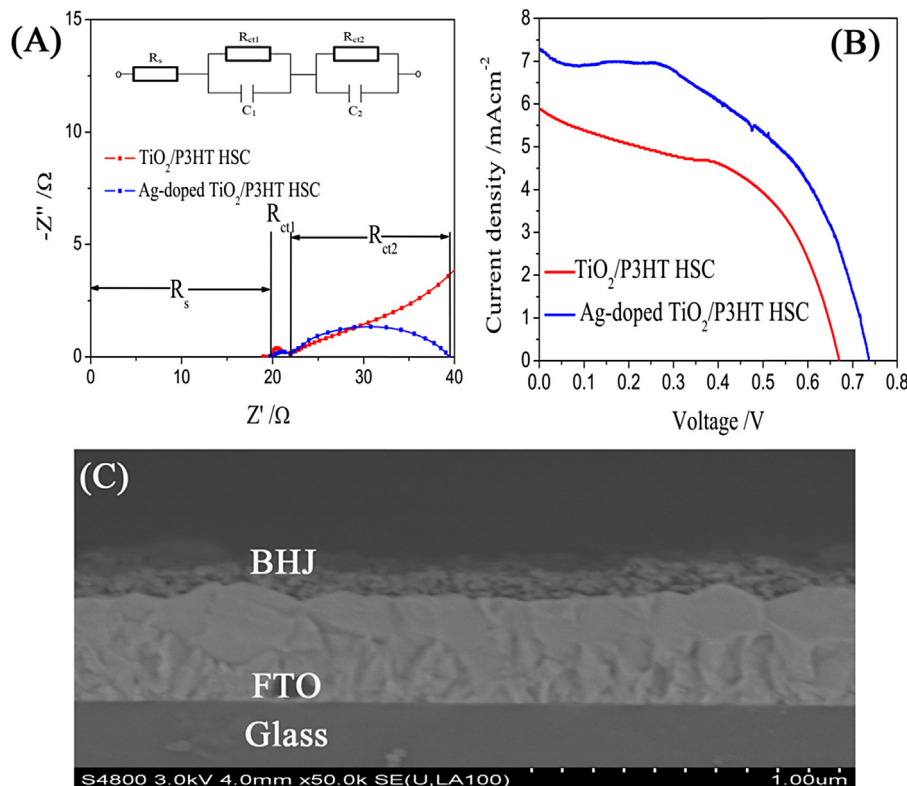


Fig. 7. (A) EIS spectra of the HSCs from bare TiO₂ and Ag-doped TiO₂ electrode and the insert denotes the equivalent circuit used to fit the impedance data; (B) *J*–*V* curves of HSCs based on different photoanode comprising of TiO₂ and Ag-doped TiO₂, respectively; (C) SEM image of cross-section of Ag-doped TiO₂/P3HT BHJ.

a standard means for the electrochemical characterization of semiconductor materials. For the n-type semiconductor, the relationship between the capacitance (*C*) and the applied potential (*V*) can be expressed by using Eq. (3) [62]:

$$C^{-2} = \frac{2}{A^2 \varepsilon \varepsilon_0 N_D} \left(V - V_{FB} - \frac{kT}{e} \right) \quad (3)$$

in which *N_D* is the doping density, *V_{FB}* is the flat-band (FB) potential, *k* is the Boltzmann constant, *T* is the temperature, *ε* is the relative dielectric constant of the anodic film, *ε₀* is the permittivity of free space, *e* is the charge of an electron, and *A* is the electrode area. The flat band potentials were determined by Mott–Schottky plots (*C*^{−2} versus *V*) as obtained by a linear extrapolation to *C* = 0, i.e., the intercept at the X axis. Then, the CB energy level was calculated with Ag/Ag⁺ as reference. The band gap was determined from the UV–vis absorption spectrum using the following relationship: *E_g* = 1240/λ eV. Finally the VB energy level was obtained and listed in Table 2. As shown in Table 3, the CB, VB and band gap *E_g* obtained from the CV characteristics are in reasonable agreement with those determined from the UV–vis and Mott–Schottky method, indicating that the results obtained in this work are reliable.

The Nyquist plots of the HSCs consisting of TiO₂ (or Ag-doped TiO₂) anode/PEDOT:PSS/Pt counter were displayed in Fig. 7A. The EIS curves of the two HSCs exhibit two semicircles: the small semicircle can be attributed to the charge transfer resistance (*R_{ct1}*) at the interface of the Pt and PEDOT:PSS while the large

semicircle represents the charge transfer resistance (*R_{ct2}*) at the interface of TiO₂ (or Ag-doped TiO₂) and PEDOT:PSS [63–65]. The EIS data were fitted numerically by the equivalence model [24], and the parameters from the best fit were summarized in Table 3. It reveals that the Ag-doped photoanode has a lower *R_{ct2}* than that without doping, i.e., 17.40 Ω vs 23.12 Ω. A lower charge transfer resistance facilitates an easier charge transfer and it ensures that the photoexcited electrons have enough time to reach the electrode before the recombination occurs [24]. With a view to exploring the doping effect on the final photovoltaic performance of HSCs, we prepared and characterized two types of BHJs for comparison: TiO₂/P3HT and Ag-doped TiO₂/P3HT blend films. The cross-section of the BHJ was characterized by SEM as shown in Fig. 7C. The thickness of BHJ layer including Ag-doped TiO₂ and P3HT was estimated to be about 200 nm. The intimate interface of BHJ was clearly observed, which can benefit an efficient charge separation in BHJ because the photoexcited charge carriers in P3HT cannot diffuse too long, typically ~12 nm [66]. Under the identical experimental conditions, the prepared HSCs with Ag doping exhibit a higher *J_{sc}* (7.28 mA/cm² vs 5.91 mA/cm²) and also a higher *V_{oc}* (0.736 V vs 0.670 V), thus leading to an enhancement of PCE by almost 38%, i.e., 2.73% as compared to its counterpart without doping (1.98%) (Fig. 5B and Table 3). However, what is held responsible for the improved photovoltaic performances? On one hand, it is known that the photocurrent depends on the efficiency of photoexcited carrier transfer and charge collection [54]. Meanwhile, the

Table 3
Photovoltaic parameters of the HSCs and EIS parameters of best fit.

BHJ	<i>V_{oc}</i> (V)	<i>J_{sc}</i> (mA cm ^{−2})	<i>FF</i>	<i>η</i> ^a (%)	<i>R_s</i> (Ω)	<i>R_{ct1}</i> (Ω)	<i>R_{ct2}</i> (Ω)
TiO ₂ /P3HT	0.670	5.91	0.50	1.98	19.65	1.93	23.12
Ag-doped TiO ₂ /P3HT	0.736	7.28	0.51	2.73	19.90	2.10	17.40

^a *η* = *J_{sc}**V_{oc}**FF*/*P_{in}*, where *P_{in}* = 100 mW cm^{−2} (AM 1.5).

enhanced J_{sc} should be ascribed to the reduction of excess CB-LUMO offset, thus shortening the electron transfer time and leading to an efficient extraction and collection of photoexcited electrons. On the other hand, the V_{oc} is governed by several factors, one of which is the energy offset between the HOMO of donor and CB edge of the acceptor as described in the theoretical equation [67]. In this work, the CB-HOMO offset has increased from 0.77 to 1.03 eV, which may provide some insight into the enhancement of V_{oc} . Therefore, the efficiency enhancement of solar cells stems from the regulation of energy level, the efficient reduction of energy offset induced by the incorporation of Ag dopants and the decreased charge transfer resistance R_{ct2} .

4. Conclusion

In conclusion, we reported the first attempt of revealing the tailoring of energy level of TiO_2 acceptor by silver ion doping and investigated the effect on the electron transport. The results show that a remarkable acceleration of photoexcited electron transfer, i.e., from 30.2 to 18.3 ps, was clearly observed. This is mainly ascribed to the reduction of excess CB-LUMO offset, i.e., from 1.33 to 1.07 eV. Moreover, the EIS curves confirm that the incorporation of Ag dopant is an effective strategy to achieve lower charge transfer resistance (17.40 Ω vs 23.12 Ω). Additionally, the HSC made from Ag-doped TiO_2 nanocrystalline exhibits better device performance in J_{sc} and V_{oc} than pure TiO_2 photoanode, thus delivering an improved PCE of 2.73% as compared to 1.98%. This work demonstrates that suitably chosen photocatalyst can have an important role in solar energy conversion and with a refined and delicate design, the excess energy offset can be reduced further. Our work provides a new route for the faster electron transfer within nanoscale photovoltaic devices and photon detectors.

Acknowledgments

The authors gratefully acknowledge the financial support of the Natural Science Foundation of China (61366003), the Science and Technology Project of the Education Department of Jiangxi Province, China (GJJ12449, GJJ12455, GJJ14533) and Aviation Science Fund of China (2013ZF56025).

References

- [1] Y. Lei, H. Jia, W. He, Y. Zhang, L. Mi, H. Hou, G. Zhu, Z. Zheng, *J. Am. Chem. Soc.* 134 (2012) 17392–17395.
- [2] J. Chandrasekaran, D. Nithyaprakash, K.B. Ajjan, S. Maruthamuthu, D. Manoharan, S. Kumar, *Renew. Sust. Energy Rev.* 15 (2011) 1228–1238.
- [3] S. Shoaee, J. Briscoe, J.R. Durrant, S. Dunn, *Adv. Mater.* 26 (2014) 263–268.
- [4] J.M. Lee, B.H. Kwon, H.I. Park, H. Kim, M.G. Kim, J.S. Park, E.S. Kim, S. Yoo, D.Y. Jeon, S.O. Kim, *Adv. Mater.* 25 (2013) 2011–2017.
- [5] B. Reeja-Jayan, A. Manthiram, *Sol. Energy Mater. Sol. Cells* 94 (2010) 907–914.
- [6] W.-F. Fu, Y. Shi, L. Wang, M.-M. Shi, H.-Y. Li, H.-Z. Chen, *Sol. Energy Mater. Sol. Cells* 117 (2013) 329–335.
- [7] Y. Liu, M.A. Summers, C. Edder, J.M.J. Fréchet, M.D. McGehee, *Adv. Mater.* 17 (2005) 2960–2964.
- [8] J. Lee, S. Mubeen, G. Hernandez-Sosa, Y. Sun, F.M. Toma, G.D. Stucky, M. Moskovits, *Adv. Mater.* 25 (2013) 256–260.
- [9] Y. Zhou, M. Eck, M. Krüger, *Energy Environ. Sci.* 3 (2010) 1851–1864.
- [10] F. Gao, S. Ren, J. Wang, *Energy Environ. Sci.* 6 (2013) 2020–2040.
- [11] Y. Wu, G. Zhang, *Nano Lett.* 10 (2010) 1628–1631.
- [12] M.J. Greaney, S. Das, D.H. Webber, S.E. Bradforth, R.L. Brutchey, *ACS Nano* 6 (2012) 4222–4230.
- [13] T. Rakshit, S.P. Mondal, I. Manna, S.K. Ray, *ACS Appl. Mater. Interfaces* 4 (2012) 6085–6095.
- [14] M. Hallermann, I. Kriegel, E. Da Como, J.M. Berger, E. von Hauff, J. Feldmann, *Adv. Funct. Mater.* 19 (2009) 3662–3668.
- [15] N. Massihi, M.R. Mohammadi, A.M. Bakhshayesh, M. Abdi-Jalebi, *Electrochim. Acta* 111 (2013) 921–929.
- [16] A.E. Shalan, M.M. Rashad, *Appl. Surf. Sci.* 283 (2013) 975–981.
- [17] T. Hori, T. Shibata, V. Kittichungchit, H. Moritou, J. Sakai, H. Kubo, A. Fujii, M. Ozaki, *Thin Solid Films* 518 (2009) 522–525.
- [18] M. Yang, L. Huo, L. Pei, K. Pan, Y. Gan, *Electrochim. Acta* 125 (2014) 288–293.
- [19] Y. Xie, N. Huang, S. You, Y. Liu, B. Sebo, L. Liang, X. Fang, W. Liu, S. Guo, X.-Z. Zhao, *J. Power Sources* 224 (2013) 168–173.
- [20] W. Nie, R.C. Coffin, D.L. Carroll, *Int. J. Photoenergy* 2013 (2013) 1–6.
- [21] L. Liu, H. Bai, J. Liu, D.D. Sun, J. Hazard. Mater. 261 (2013) 214–223.
- [22] H. Zhang, C. Liang, J. Liu, Z. Tian, G. Wang, W. Cai, *Langmuir* 28 (2012) 3938–3944.
- [23] R. Liu, P. Wang, X. Wang, H. Yu, J. Yu, *J. Phys. Chem. C* 116 (2012) 17721–17728.
- [24] B. Sebo, N. Huang, Y. Liu, Q. Tai, L. Liang, H. Hu, S. Xu, X.-Z. Zhao, *Electrochim. Acta* 112 (2013) 458–464.
- [25] G. Xu, H. Liu, J. Wang, J. Lv, Z. Zheng, Y. Wu, *Electrochim. Acta* 121 (2014) 194–202.
- [26] M. Sun, W. Fu, H. Yang, Y. Sui, B. Zhao, G. Yin, Q. Li, H. Zhao, G. Zou, *Electrochim. Commun.* 13 (2011) 1324–1327.
- [27] J.-H. Qi, Y. Li, T.-T. Duong, H.-J. Choi, S.-G. Yoon, *J. Alloys Compd.* 556 (2013) 121–126.
- [28] E.A. Parlak, T. Aslı Tumay, N. Tore, Ş. Sarioğlu, P. Kavak, F. Türksöy, *Sol. Energy Mater. Sol. Cells* 110 (2013) 58–62.
- [29] C.L. Haynes, R.P. Van Duyne, *J. Phys. Chem. B* 107 (2003) 7426–7433.
- [30] D. Credgington, F.C. Jamieson, B. Walker, T.Q. Nguyen, J.R. Durrant, *Adv. Mater.* 24 (2012) 2135–2141.
- [31] W.A. Tisdale, K.J. Williams, B.A. Timp, D.J. Norris, E.S. Aydil, X.Y. Zhu, *Science* 328 (2010) 1543–1547.
- [32] J. Wu, S. Hao, J. Lin, M. Huang, Y. Huang, Z. Lan, P. Li, *Cryst. Growth Des.* 8 (2007) 247–252.
- [33] J. Wu, S. Hao, Z. Lan, J. Lin, M. Huang, Y. Huang, P. Li, S. Yin, T. Sato, *J. Am. Chem. Soc.* 130 (2008) 11568–11569.
- [34] N.A.M. Barakat, M.A. Kanjwal, I.S. Chronakis, H.Y. Kim, *J. Mol. Catal. A: Chem.* 366 (2013) 333–340.
- [35] M. Grätzel, *Inorg. Chem.* 44 (2005) 6841–6851.
- [36] W.F. Sun, Q.H. Zeng, A.B. Yu, *Langmuir* 29 (2013) 2175–2184.
- [37] W.F. Sun, Q.H. Zeng, A.B. Yu, K. Kendall, *Langmuir* 29 (2013) 7825–7837.
- [38] W.F. Sun, *Nanoscale* 5 (2013) 12658–12669.
- [39] W.F. Sun, *Phys. Chem. Chem. Phys.* 16 (2014) 5846–5854.
- [40] Q. Li, J. Wu, Q. Tang, Z. Lan, P. Li, J. Lin, L. Fan, *Electrochim. Commun.* 10 (2008) 1299–1302.
- [41] Q. Li, H. Chen, L. Lin, P. Li, Y. Qin, M. Li, B. He, L. Chu, Q. Tang, *J. Mater. Chem. A* 1 (2013) 5326–5332.
- [42] W.F. Sun, G.H. Chen, L.L. Zheng, *Scr. Mater.* 59 (2008) 1031–1034.
- [43] H. Acharya, J. Sung, B.-H. Sohn, D.H. Kim, K. Tamada, C. Park, *Chem. Mater.* 21 (2009) 4248–4255.
- [44] R. Sanjinés, H. Tang, H. Berger, F. Gozzo, G. Margaritondo, F. Lévy, *J. Appl. Phys.* 75 (1994) 2945–2951.
- [45] G. Xing, N. Mathews, S. Sun, S.S. Lim, Y.M. Lam, M. Gratzel, S. Mhaisalkar, T.C. Sum, *Science* 342 (2013) 344–347.
- [46] W.J.E. Beek, M.M. Wienk, R.A.J. Janssen, *Adv. Funct. Mater.* 16 (2006) 1112–1116.
- [47] J.K.J. van Duren, X. Yang, J. Loos, C.W.T. Bulle-Lieuwma, A.B. Sieval, J.C. Hummelen, R.A.J. Janssen, *Adv. Funct. Mater.* 14 (2004) 425–434.
- [48] S. Cook, A. Furube, R. Katoh, *Energy Environ. Sci.* 1 (2008) 294–299.
- [49] B. Ferreira, P.F. da Silva, J.S. Seixas de Melo, J. Pina, A. Maçanita, *J. Phys. Chem. B* 116 (2012) 2347–2355.
- [50] B. Kraabel, D. Moses, A.J. Heeger, *J. Chem. Phys.* 103 (1995) 5102–5108.
- [51] S.D. Stranks, G.E. Eperon, G. Grancini, C. Menelaou, M.J. Alcocer, T. Leijtens, L.M. Herz, A. Petrozza, H.J. Snaith, *Science* 342 (2013) 341–344.
- [52] R.A. Marsh, J.M. Hodgkiss, S. Albert-Seifried, R.H. Friend, *Nano Lett.* 10 (2010) 923–930.
- [53] H. Ohkita, S. Ito, *Polymer* 52 (2011) 4397–4417.
- [54] T.M. Clarke, J.R. Durrant, *Chem. Rev.* 110 (2010) 6736–6767.
- [55] D. McMorro, W.T. Lotshaw, G.A. Kenney-Wallace, *IEEE J. Quantum Electron.* 24 (1988) 443–454.
- [56] D. McMorro, W.T. Lotshaw, *J. Phys. Chem.* 95 (1991) 10395–10406.
- [57] X. Gong, M. Tong, F.G. Brunetti, J. Seo, Y. Sun, D. Moses, F. Wudl, A.J. Heeger, *Adv. Mater.* 23 (2011) 2272–2277.
- [58] I. Mora-Sero, L. Bertoluzzi, V. Gonzalez-Pedro, S. Gimenez, F. Fabregat-Santiago, K.W. Kemp, E.H. Sargent, J. Bisquert, *Nat. Commun.* 4 (2013) 2272.
- [59] Y.C. Li, H.Z. Zhong, R. Li, Y. Zhou, C.H. Yang, Y.F. Li, *Adv. Funct. Mater.* 16 (2006) 1705–1716.
- [60] W. Li, W.S. Roelofs, M.M. Wienk, R.A. Janssen, *J. Am. Chem. Soc.* 134 (2012) 13787–13795.
- [61] B. Yang, Y. Yuan, P. Sharma, S. Poddar, R. Korlacki, S. Ducharme, A. Gruverman, R. Saraf, J. Huang, *Adv. Mater.* 24 (2012) 1455–1460.
- [62] J.L. Wang, J.H. Wu, J.M. Lin, M.L. Huang, Y.F. Huang, Z. Lan, Y.M. Xiao, G.T. Yue, S. Yin, T. Sato, *ChemSusChem* 5 (2012) 1307–1312.
- [63] B. He, Q. Tang, M. Wang, C. Ma, S. Yuan, *J. Power Sources* 256 (2014) 8–13.
- [64] Q. Li, Q. Tang, N. Du, Y. Qin, J. Xiao, B. He, H. Chen, L. Chu, *J. Power Sources* 248 (2014) 816–821.
- [65] S. Yuan, Q. Tang, B. He, L. Men, H. Chen, *Electrochim. Acta* 125 (2014) 646–651.
- [66] P.E. Shaw, A. Ruseckas, I.D.W. Samuel, *Adv. Mater.* 20 (2008) 3516–3520.
- [67] R. Kroon, M. Lenes, J.C. Hummelen, P.W.M. Blom, B. de Boer, *Polym. Rev.* 48 (2008) 531–582.